The Role of Surface Hydroxyls in the Entropy Driven Adsorption and Spillover of H_2 on Au/TiO_2 Catalysts

Authors: Akbar Mahdavi-Shakib,[1]† Todd N. Whittaker,[2,3]† Tae Yong Yun,[1] K. B. Sravan Kumar,[4]‡ Lauren C. Rich,[2] Shengguang Wang,[4] Robert M. Rioux,[1,5] Lars C. Grabow,[,4,6] and Bert D. Chandler[1,5]

Affiliations:

[1]Department of Chemical Engineering, The Pennsylvania State University, University Park, Pennsylvania 16802, United States

[2]Department of Chemistry, Trinity University, San Antonio, Texas 78212-7200, United States

[3]Department of Chemical and Biological Engineering, The University of Colorado, Boulder, Colorado 80303, United States

[4]Department of Chemical and Biomolecular Engineering, University of Houston, Houston, TX 77204-4004

[5]Department of Chemistry, The Pennsylvania State University, University Park, Pennsylvania 16802, United States

[6]Texas Center for Superconductivity at the University of Houston (TcSUH), University of Houston, Houston, TX 77204

*Corresponding author. Email: bert.chandler@psu.edu

†These authors contributed equally to this paper and project.

‡ Current address: Umicore AG & Co. KG, 63457 Hanau, Germany

Abstract: Hydrogen spillover involves the migration of H atom equivalents from metal nanoparticles to a support. While well-documented, H spillover is poorly understood and largely unquantified. Here, we measure weak, reversible H_2 adsorption on Au/TiO_2 catalysts, and extract the surface concentration of spilled-over hydrogen. The spillover species (H*) is best described as a loosely coupled proton/electron pair distributed across the titania surface hydroxyls. In stark contrast to traditional gas adsorption systems, H* adsorption increases with temperature. This unexpected adsorption behavior has two origins. First, entropically favorable adsorption results from high proton mobility and configurational surface entropy. Second, the number of spillover sites increases with temperature, due to increasing hydroxyl acid-base equilibrium constants. Increased H* adsorption correlates with the associated changes in titania surface zwitterion concentration This study provides a quantitative assessment of how hydroxyl surface chemistry impacts spillover thermodynamics, and contributes to the general understanding of spillover phenomena.

Introduction

Hydrogen spillover, which transfers hydrogen atom equivalents from a metal nanoparticle to an oxide support,[1-3] is a well-documented phenomenon that bridges heterogeneous catalysis, semiconductor surface chemistry, and photo-/electro-catalytic hydrogen evolution.[3-8] It has broad technological impacts including H_2 production, utilization, and storage systems; accordingly, spillover will likely be pivotal in reducing CO_2 emissions. Various descriptions of spillover are invoked for a broad array of materials, including single atom alloys,[9-11] high entropy alloys, [12] metal-organic frameworks,[13] and metal-semiconductor photoelectrodes.[14,15]

For supported metal catalysts, spillover onto oxide supports is strongly associated with support reducibility, as reducible supports show spillover effects over far larger distances than non-reducible supports.[1] In these systems, spillover originates at the metal-support interface (MSI), which participates in numerous catalytic reactions.[16-18] The MSI is especially important for supported Au catalysts,[19,20] which are highly active for a variety of catalytic oxidations[20-23] and highly selective in organic synthesis.[24-26]

Gold catalysts display a surprising dichotomy in reactions involving H_2. Au/TiO_2 is highly active for formic acid dehydrogenation,[27] photocatalytic H_2 evolution,[4-6] and water-gas shift chemistries,[28,29] yet Au catalysts have only moderate activity in several important selective and partial hydrogenations, and are nearly inert in alkene hydrogenation.[30] This distinctive reactivity is associated with the relative inertness of Au surfaces and its consequence for H_2 activation. While most metals activate H_2 through strong dissociative chemisorption, H_2 adsorption on Au metal is thermodynamically unfavorable.[31-33] As a result, supported Au catalysts activate H_2 at the MSI via an entirely separate mechanism: heterolytic H_2 activation followed by fast Au-H deprotonation.[33-35]

We recently showed the notoriously weak H_2 adsorption on Au/TiO_2 yields two H-atom equivalents (2 protons and 2 electrons) localized on MSI hydroxyls: there are essentially no Au-H species on the catalyst.[32-35] Additionally, Au/TiO_2 catalysts continue to adsorb hydrogen long after the adsorption sites are saturated.[35] As we show conclusively below, the increased surface coverage is due to hydrogen spillover.

Despite its technological importance, spillover remains poorly understood and largely unquantified, for two primary reasons.[3] First, it is difficult to distinguish spillover from weak H adsorption on active metal surfaces. Second, it is difficult to disentangle spillover from the effects of especially support reduction and the strong metal-support interaction. Indeed, spillover is often referred to interchangeably with support reduction, complicating their discussion in the literature.[2] While there is no universal definition of spillover, we defer to Prins' distinction between spillover, which is highly mobile H-atom equivalents (H*), and reversible support reduction which has the effect of storing spilled-over H within an oxide support. As Prins' review details, these are related, but fundamentally distinct processes.

While support reduction can be quantified by several methods, the inability to quantify the mobile H* species that lead to support reduction has been a key limitation to studying spillover. With essentially no H adsorption on Au, H_2 adsorption on Au/TiO_2 provides an ideal platform to quantify these difficult to study species. As we show below, spillover results from several unexpected adsorption phenomena that break several traditional assumptions regarding gas-phase adsorption. These include the conclusion that spillover is an entropy driven adsorption process in which the number of adsorption sites increases with temperature.

Results

Quantifying Hydrogen Spillover. H_2 adsorption on Au/TiO_2 is both fast and reversible, with an activation barrier of ~20 kJ/mol.[33-35] Reversible H_2 adsorption isotherms, measured directly with a combination of volumetric chemisorption and IR spectroscopy, show the quantity of adsorbed hydrogen roughly doubles as the adsorption temperature increases from 50 to 150 °C (**Figure 1A**). The adsorption isotherms are highly reproducible, and we collected similar data on more than a dozen separate batches of catalyst. Because this is weak, reversible adsorption the anomalous temperature dependence cannot be attributed to activated adsorption, as is well-known for N_2 adsorption in ammonia synthesis.[36] We also confirmed no surface species (i.e., water) are released upon adsorption, as this can drive adsorption at higher temperatures (see Supplementary **Figure 3**).[37]

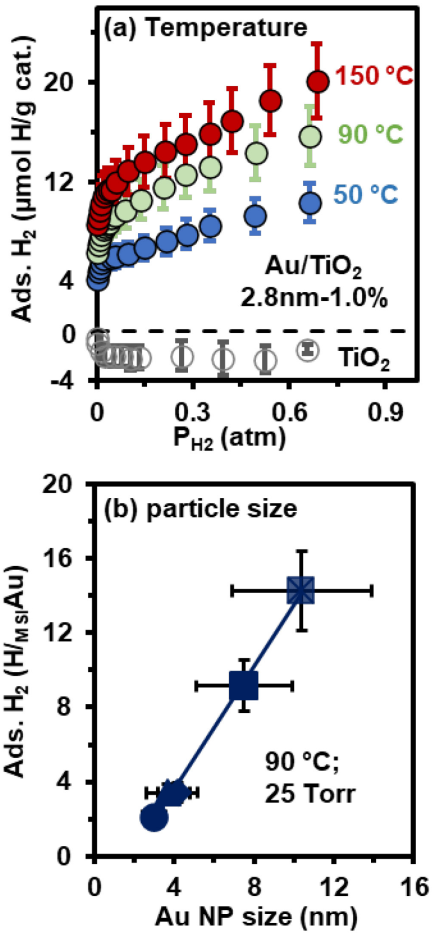

Figure 1. Temperature and particle size effects on H_2 adsorption. (a) H_2 equilibrium adsorption isotherms on Au/TiO_2 as a function of temperature and P_{H2}. Error bars show the standard deviation based on at least four isotherm measurements. **(b)** Total H_2 adsorption normalized to the number of MSI sites as a function of Au particle size. At a constant Au wt. %, H_2 adsorption per adsorption site increases with Au particle size. Error bars show standard deviations from TEM data (x-axis) and adsorption isotherm data (y-axis). Particle size calculations are detailed in the **Supplementary Methods**.

The isotherms quantify the total amount of adsorbed H (H_{tot}), so quantifying H* requires accounting for different adsorption sites. Previous work shows there is one reactive support hydroxyl ($_{MSI}$TiOH) per perimeter Au atom ($_{MSI}$Au). The $_{MSI}$TiOHs (surface concentration = 1.8 μmol / g cat.) are the strongest H-atom binding sites on the catalyst; further, they are always occupied under H_2[33] and remain saturated with H_2 up to at least 120 °C (**Figure S5**). **Figure 1B** shows H_{tot} far exceeds the number of adsorption sites; most of the adsorbed H_2 must therefore migrate either to the Au nanoparticle or the TiO_2 support.

Hydrogen adsorption on extended Au surfaces is thermodynamically unfavorable.[31-33] Smaller Au particles are generally more reactive; the increase in H_{ads} with Au particle size (**Figure 1B**) suggests the excess H is transferred to the support. To test this, we prepared catalysts with constant particle size (3 ± 0.2 nm) but varied Au loading. If the additional H_{ads} is transferred to Au, the H/Au_{surf} ratio should be constant for these catalysts. **Figure 2a** shows the H/Au_{surf} ratio changes by a factor of three, ruling out H transfer to Au_{surf} and confirming the additional H_{ads} is H* on the support.

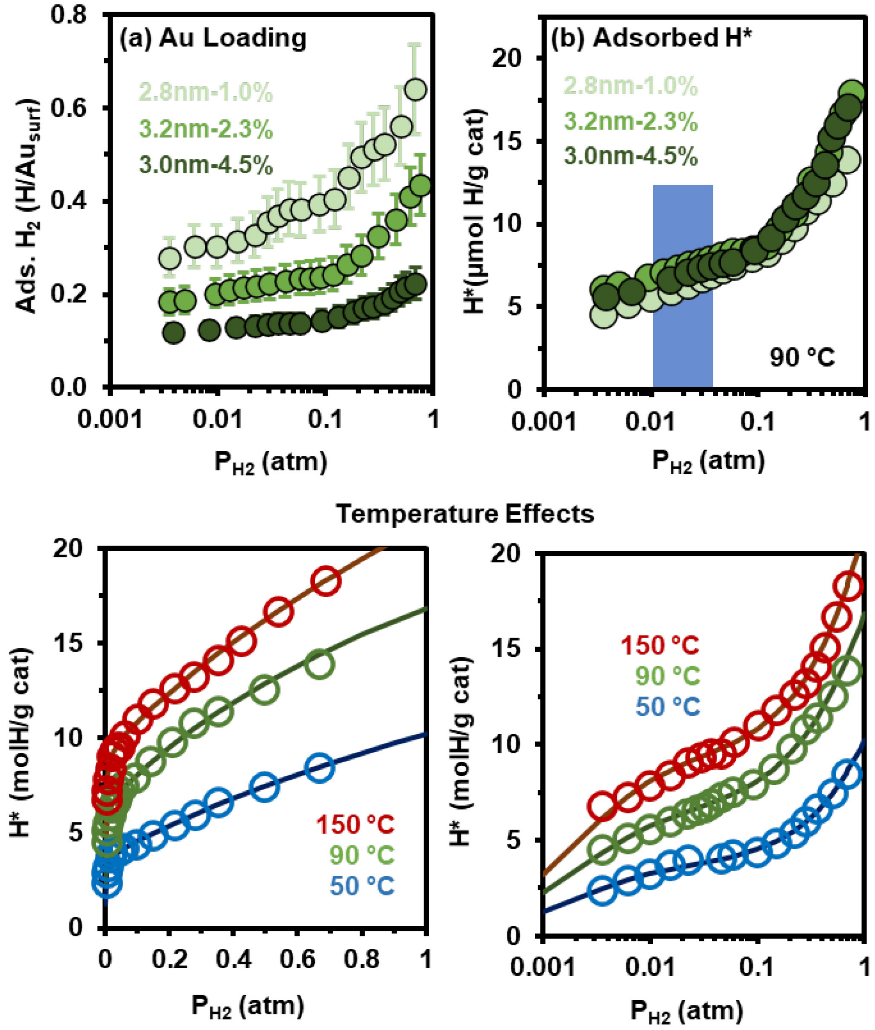

Figure 2. Au loading effects on H_2 adsorption and spillover. (a) H_2 adsorption isotherms (90 °C) on catalysts with comparable Au particle size (~3 nm), but variable Au loading. Total H_{ads} is normalized to the number of surface Au atoms; the ratio of H_{ads}:Au_{surf} changes with Au loading indicating H is not transferred to Au. **(b)** H* adsorption isotherms; data from 2A with adsorption attributable to the MSI sites subtracted. **(c & d)** Temperature effects on H* adsorption; data from

1A with adsorption attributable to the MSI sites subtracted plotted on linear (c and logarithmic (d axes. Lines are fits to two-site Langmuir models.

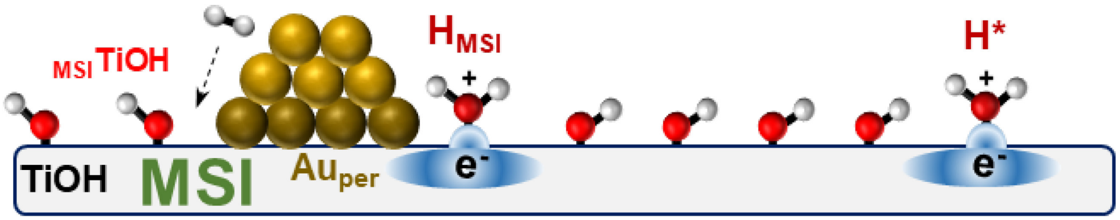

Figure 3. Schematic showing H_2 adsorption at the MSI. Beginning from the left of the figure, H_2 adsorbs at the Au/TiO_2 metal-support interface (MSI). The species adsorbed at the interface (H_{MSI}), is described as a proton interacting with a basic MSI hydroxyl group and an electron delocalized across the associated Ti-O antibonding orbital, nearby support atoms, and the Au. Once the MSI hydroxyls are saturated with HMSI, H-atom equivalents (H*) are transferred to the support. The highly mobile H* species are similar to HMSI, consisting of a proton interacting with a surface TiOH and an electron in surface conduction band states delocalized across the TiOH and neighboring support atoms.

These measurements are enabled by the unique properties of Au/TiO_2. There is no H_2 chemisorption on Au and no measurable H_2 physisorption on TiO_2 (**Figure 1A**, grey data). Thus, weak H_2 adsorption can be attributed to H_{MSI} and H*, shown schematically in **Figure 3.** Because the MSI sites are always occupied in these experiments, [34] H* isotherms can be determined by subtracting H_{MSI} from H_{tot} at each equilibrium pressure, as described in section 5 of the **SI**. [34] **Figure 2B** shows the resulting isotherms are independent of the Au loading, further confirming spillover to the TiO_2 support. Similarly, **Figure 2C** shows the increase in H adsorption with temperature in **Figure 1A** is attributable to increases in H*. To our knowledge, these are the first reported isotherms for weakly adsorbed, mobile hydrogen spillover.

Langmuir Analyses. The H* adsorption isotherms do not fit a single Langmuir adsorption isotherm, indicating the free energy for adsorption (ΔG_{H*}) changes substantially with surface concentration. The experimental data fit Freundlich isotherms, but these power-law fits have no physical basis and therefore provide limited utility for understanding the adsorption phenomenon.

The H* isotherms are well described with multi-site Langmuir models. Fits to a simple two-site Langmuir models are included in **Figure 2C**; further details are provided in the **Supplementary Discussion**. We also used a progressive Langmuir analysis as shown in **Figure 4A**. This treatment plots adsorption data in a linearized form of the Langmuir equation. While the full data set is not linear due to the coverage dependent adsorption energy, the plot is linear over small pressure ranges where changes in surface concentration are small. Under these conditions, K_{ads} is relatively constant, and the Langmuir approximation is valid. This treatment generates two descriptive parameters for each pressure range: (i) the adsorption equilibrium constant (K_P^*, where P indicates the median pressure used) and (ii) a surface H* concentration ($_{surf}C_P^*$) which quantifies the adsorption capacity for the pressure range, i.e. the number H* adsorbates with $K_{ads}^* \geq K_P^*$.

Both methods do a good job of describing individual isotherms. The two-site model condenses the coverage dependence into strong and weak adsorption sites, simplifying the description.[38] The progressive Langmuir analysis determines multiple adsorption parameters over consecutive small pressure ranges, therefore describing the coverage dependence in greater detail.

This allows us to examine changes to the adsorption equilibrium, and therefore adsorption energetics, as a function of the H* surface concentration. This is qualitatively similar to the Temkin isotherm, but without the restriction of a linear change in adsorption energy with coverage.

This analysis (2.8 nm-1% Au/TiO$_2$ at 90 °C, **Figure 4B**) shows H* adsorption strength decreases substantially as H* surface concentration increases. **Supplementary Tables 3-6** compile extracted adsorption parameters for 5 different catalysts and 4 adsorption temperatures. To facilitate discussions, we discuss adsorption parameters determined at 25 Torr as representative of the broader trends. The K_{25}^* and ${}_{surf}C_{25}^*$ values are remarkably consistent across all catalysts, indicating the H* surface concentration is independent of Au particle size or loading. This further confirms H* is associated with the support.

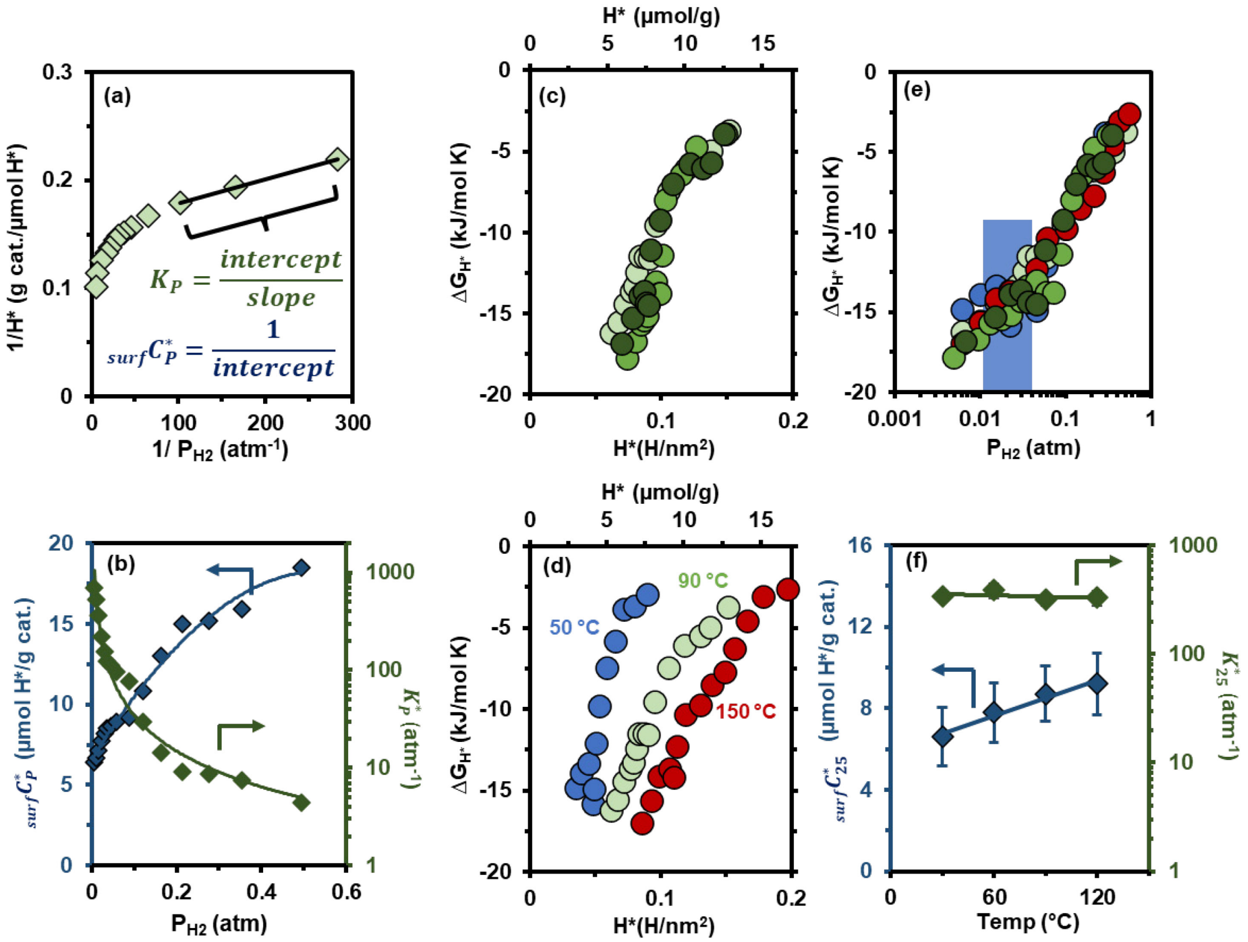

Figure 4. H* Adsorption Thermodynamics. (**a**) Linearized Langmuir plot for H* on 2.8 nm-1% Au/TiO$_2$ at 90 °C. Langmuir parameters were extracted from sliding linear fits as shown. (**b**) Extracted Langmuir parameters from (A) plotted as a function of P$_{H2}$. Data show the adsorption equilibrium has a strong surface concentration dependence. (**c**) ΔG$_{H*}$ values at 90 °C for three catalysts as a function of surface concentration. (**d**) ΔG$_{H*}$ values for 2.8 nm-1% Au/TiO$_2$ at three temperatures. (**e**) Data from panels (C) and (D) plotted versus P$_{H2}$. **(f)** Langmuir parameter temperature dependence. Parameters extracted at ~25 Torr H$_2$; symbols average 5 data points measured over 5 different catalysts having different Au loadings and average particle sizes between 2.5 and 4 nm. Error bars show standard deviations for at least 5 determinations over 5

different catalysts with varying Au loading and particle size (minimum 15 measurements); error bars for K^*_{25} values are smaller than the symbols (RSD: 12%).

Adsorption Energetics. **Figure 4C** shows ΔG_{H*} values extracted from the isotherms in **Figure 2B**; ΔG_{H*} values vary by ~20 kJ/mol and are consistent with weak adsorption. Plots of ΔG_{H*} vs H* surface concentration for this data are in **Figure 4D**. At any given surface concentration, ΔG_{H*} becomes more favorable as temperature increases. However, when the same data is plotted as ΔG_{H*} vs. P_{H2} (**Figure 4E**) adsorption energies show the same pressure dependence and are indistinguishable from the catalysts with different Au loadings. This is remarkable behavior with little precedent in the adsorption literature. As we detail below, it is consistent with an increase in adsorption sites with increasing temperature.

To examine this possibility, we plotted the extracted Langmuir parameters vs. temperature, focusing on the data collected at 25 Torr to simplify quantitative comparisons. **Figure 4F** shows K^*_{25} is constant with temperature, consistent with **Figure 4E**. Simultaneously the "maximum" surface concentration (${}_{surf}C^*_{25}$) increases by ~50%, indicating the number of adsorption sites increases with increasing temperature. The data in Figure 4E largely represent the strong sites in the two-site Langmuir model; the weak sites show the same temperature dependence: K remains constant while the number of sites increases with temperature (**SI** section 9). Van't Hoff analysis (**SI** section 5) yields a thermoneutral adsorption enthalpy ($\Delta H_{ads} = 0 \pm 2$ kJ/mol) and a favorable adsorption entropy ($\Delta S_{ads} = +49 \pm 6$ J/mol K). Thus, H* adsorption involves two properties distinct from traditional adsorption models: a temperature-dependent change in the number of accessible adsorption sites and entropy driven adsorption.

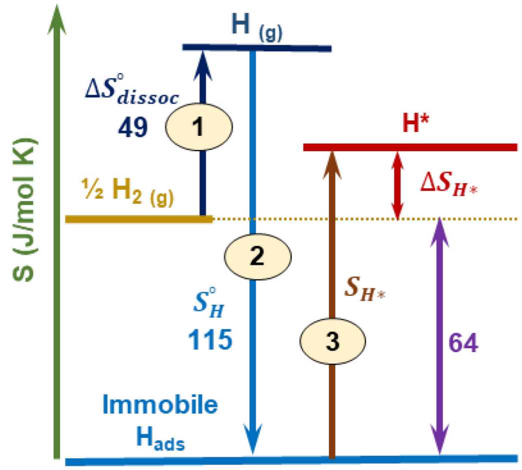

Figure 5. Entropy diagram for H* adsorption at 25 °C. Energy diagram showing changes in standard entropy for H_2 dissociation and adsorption on a solid. The entropy loss due to H atom immobilization on the surface is balanced offset by the entropy gains due to H-H bond dissociation and H surface entropy (translational, configurational, and vibrational entropy). When the standard surface entropy of the adsorbed H atoms exceeds 64 J/molK,H adsorption is entropically favorable.

Entropy Driven Adsorption. Adsorption entropies are of fundamental importance and increasing interest,[39-43] but their influences are often obscured by large enthalpic contributions to the free energy. The adsorption enthalpy for H_2 on Au/TiO_2 is approximately 0, providing an ideal opportunity to experimentally study adsorption entropy. We first address the entropic driving force, following Vannice's two-step dissociative adsorption procedure for calculating ΔS_{ads} (see **SI** section 7).[44] As **Figure 5** shows, we consider gas-phase H_2 dissociation $(1, \Delta S^{\circ}_{dissoc})$ followed by adsorption conceptualized as the loss of all gas-phase entropy $(2,\ -S^{\circ}_{H})$. The entropy of the adsorbed species $(3,\ S_{H*})$ is added to determine the adsorption entropy change (ΔS_{H*}). Since dissociation doubles the number of species, S_{H*} need only exceed 64 J/mol K for an entropically favorable process ($\Delta S_{H*} > 0$).

As Campbell et al.'s work succinctly articulates, adsorbate surface entropy is coverage dependent, comprised of translational, configurational, and vibrational components.[39,40] Based on the number or additional vibrational modes, the maximum vibrational entropy is 12 J/mol K (details in the SI). This value is small relative to the observed changes and reasonable experimental uncertainty, so vibrational entropy effects are excluded from the following analysis. Both Vannice and Campbell quantify translational entropy (${}_{tr}S$) by treating the adsorbate as a 2D ideal gas with modified versions of the Sackur-Tetrode equation.[39,40] We use a slightly modified version of Vannice's treatment (details in the **SI**), describing ${}_{tr}S$ with equation (1):

$$S_{tr} = Rln(aMT\beta) \qquad (1)$$

Where M = molar mass, T = absolute temperature, and α = the area available to each adsorbate, which is simply the inverse of the H* surface concentration. The β term is a collection of fundamental constants; for α values expressed in units of nm^2 per adsorbate, β has a value of 2.42328 $mol/g\cdot K\cdot nm^2$ (details in the **Supplementary Discussion**). This equation is not specific to H* and can be used to determine the translational entropy of any adsorbate on any surface over which it can move, provided the adsorbate is a free translator, with diffusion barrier parallel to the surface < kT.

The lines in **Figure 6A** are ${}_{tr}S_{H*}$ values calculated at three temperatures. At any given temperature, ${}_{tr}S_{H*}$ depends only on the surface concentration, reflecting the area over which each adsorbate can freely traverse; it is conceptually analogous to pressure of a 3D gas. At low surface concentrations, adsorbates move over large areas and ${}_{tr}S_{H*}$ exceeds 100 J/mol K. This is sufficient to drive H_2 adsorption. Conceptually, at the low surface densities H*, the loss of one gas-phase translational degree of freedom from H_2 is compensated by the doubling of adsorbed species and the large 2D translational area.

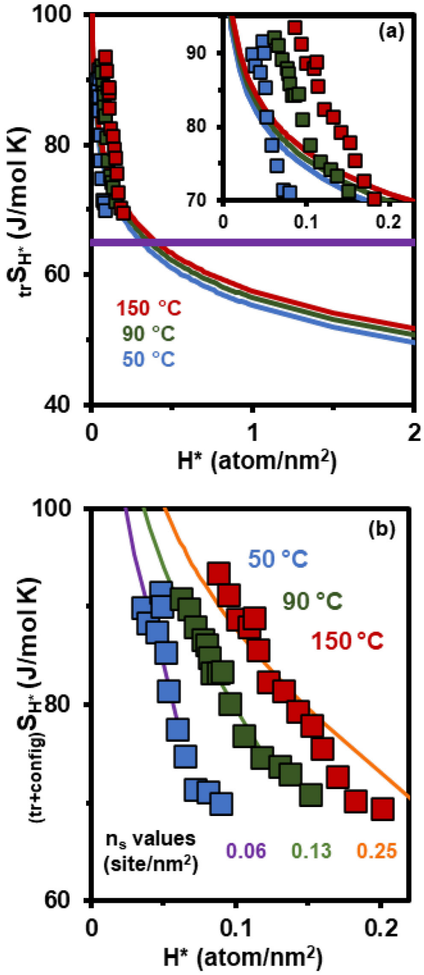

Figure 6. Entropic contributions to hydrogen spillover energetics. **(a)** Experimentally determined (symbols) and calculated (lines) S_{H^*} values based only on translational entropy contributions (${}_{tr}S_{H^*}$). The horizontal line approximates the minimum S_{H^*} required for a net favorable adsorption entropy ($\Delta S_{H^*} = 0$) at 25 °C. The inset shows the same plot at experimentally relevant H* surface densities. **(b)** Experimentally determined (symbols) and calculated (lines) S_{H^*} values including translational and configurational entropy contributions (${}_{(tr+config)}S_{H^*}$), see the **Supplementary Discussion** for details. The lines show the calculated S_{H^*} values at a specific temperature using a fitted number of adsorption sites (n_s), which is required to determine the fractional coverage see equation (2).

Experimental $\Delta S_{H^*}(\theta)$ values determined from the ΔG_{H^*} values (**Figure 4d**) show the same trend as calculated ${}_{tr}S_{H^*}(\theta)$ values. Closer examination (**Figure 6a inset**) reveals the ${}_{tr}S$ values vary minimally with temperature. While translational entropy is sufficient to explain entropy driven adsorption, it cannot account for the higher surface concentration (more H*) at higher temperatures. We therefore considered configurational entropy (${}_{config}S_{H^*}$), which is immaterial in a 3D gas, but arises from surface-adsorbate interactions. This is conceptually analogous to the difference between He and H_2 gas: the interaction between H atoms gives rise to vibrational and rotational entropies that are not present in He.

Using Campbell's hindered translator model, [39] configurational entropy is described by:

$$ {}_{config}S = R\left[ln\left(\frac{1-\theta}{\theta}\right) - \frac{ln(1-\theta)}{\theta}\right] \qquad (2)$$

Fractional coverage (θ) is required and conventionally defined as $\theta = \frac{n_{H*}}{n_S}$ where n_{H*} is the H* surface concentration and n_s is the adsorption site density. Quantifying ${}_{\mathrm{config}}S_{H*}$ requires estimating the number of available adsorption sites. **Figure 6b** shows ${}_{(\mathrm{tr+config})}S_{H*}$ values fitted to reasonable n_s values. The model only describes the experimental data if the adsorption site density (n_s, sites/nm^2) increases with temperature.

Nature of Spillover Hydrogen. Spillover is primarily associated with semiconducting supports, so we considered electronic explanations.[1,3] However, the population of surface conduction band states increases with temperature (**Supplementary Discussion**), which should inhibit H* adsorption. Previous DFT calculations indicate H_{MSI} can be described as ${}_{MSI}TiOH_2^+$, accompanied by an electron delocalized across ${}_{MSI}TiOH_2^+$, the Au nanorod, and nearby lattice O and Ti atoms. [33]

Infrared spectroscopy shows electron transfer to the support induces a broad background absorbance (BBA) associated with electron transfer to the support. [33-35] Morris [6] and Zaera [4] independently described comparable spectroscopic signals arising from H interacting with TiO_2 photocatalysts.[6] The BBA signals associated with H_{MSI} and H* are indistinguishable, indicating the two species are chemically similar. The interaction between ${}_{MSI}TiOH$ and the Au particles have allowed us to identify and assign IR signals to stretching and bending modes of $TiOH_2^+$; [34] however, no comparable signals for H* are observable.

DFT calculations on rutile (110) and anatase (001) at various coverages provide further insight into the nature of H*. Electron density difference plots at 0.1 H^+/e^- per nm^2 (**Figure 7a**) show a proton coordinated to a basic surface hydroxyl ($TiOH_2^+$). A concomitant lengthening of the Ti-O bond is observed, along with Bader charge analysis showing a net positive charge of ca. 2/3 $|e^-|$, which is assigned to the OH_2 group. This suggests charge localization on the O atom only partially balances about 1/3 of the proton charge.

Spin density difference analysis (**Figure 7b**) shows the remaining fraction of the accompanying electron is widely delocalized across multiple subsurface Ti atoms, even at the low surface concentrations comparable to experimental observations (rutile at 0.1 H^+/e^- per nm^2). With increasing surface concentrations (anatase with 1.7 H^+/e^- and rutile with 2.5 H^+/e^- per nm^2), spin density difference analysis (**Figure 7d** and **7f**) shows greater electron localization on terminal hydroxyl sites, changing their character from a formal Ti^{4+} to Ti^{3+} cation. This is similar to VandeVondele and coworkers' conclusions for spillover calculations on Pt/TiO_2[45] and with our calculations for H_{MSI}.[33]

Accordingly, H* is best described as a loosely coupled H^+/e^- pair,[3] in which the adsorption sites are tied to both support electronic properties and surface proton transfer chemistry. The system is likely highly dynamic, consistent with rapid H/D exchange.[35] The broad electron delocalization at experimentally relevant surface concentrations suggests electron stabilization, while necessary, is of secondary importance. This is consistent with our kinetic observations for H_2 activation at the MSI, where electron transfer from Au to the support follows rate-determining proton transfer. [33] This paints a broadly consistent picture of the spillover phenomenon: dynamic adsorption sites are dominated by the ability to stabilize surface protons; associated electronic effects respond to and modify the adsorption sites.

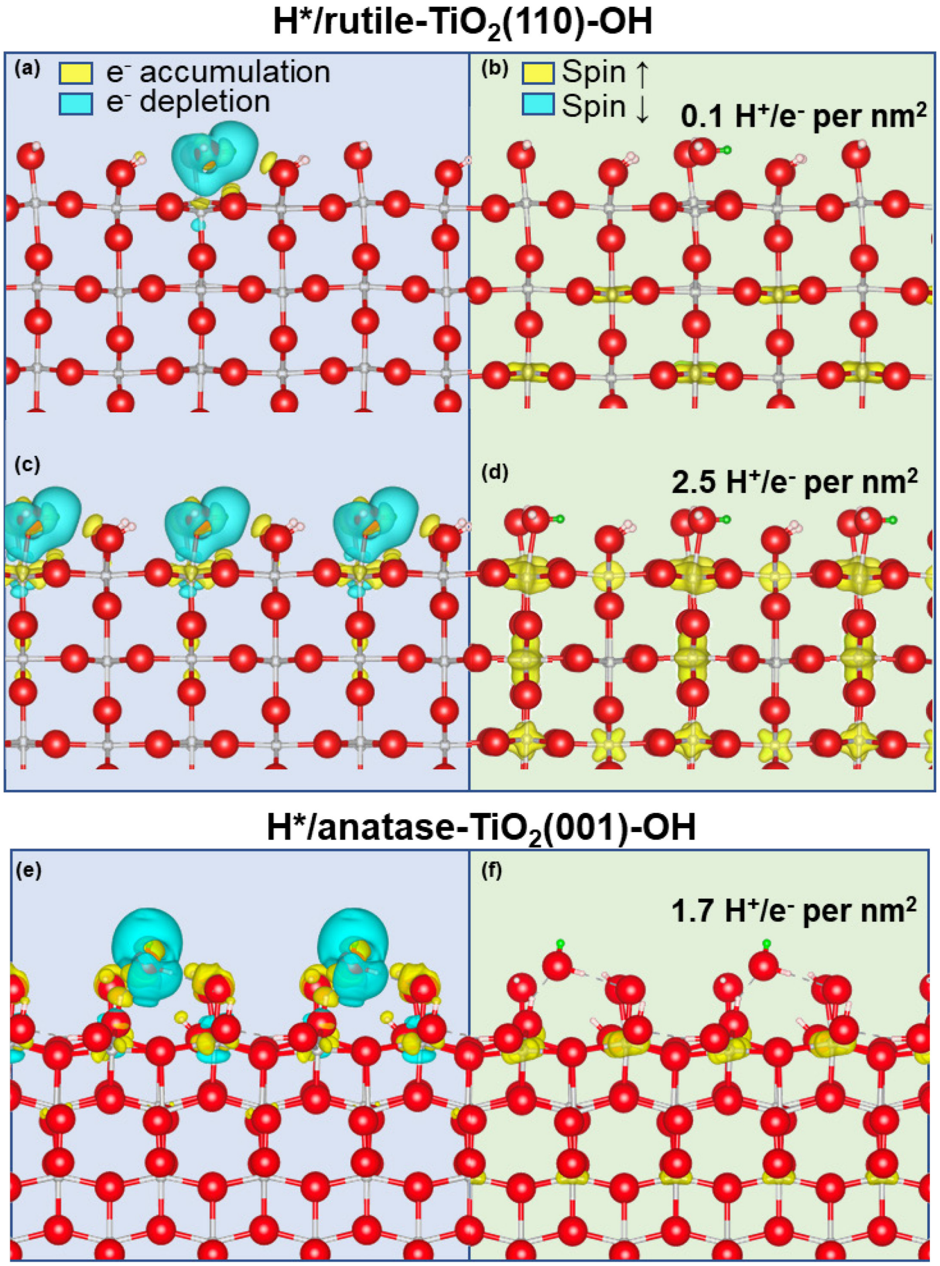

Figure 7. DFT model for H* adsorbed on rutile (110) and anatase (001). DFT calculations for H* adsorbed on fully hydroxylated rutile (110) at 0.1 H*/nm^2 (a & b), 2.5 H*/nm^2 (c & d), and anatase at 1.7 H*/nm^2 (e & f). Panels a, c, and e show changes in electron density; panels b, d, and f show changes in electron spin density.

Surface Hydroxyl Autodissociation. The surface hydroxyl density (~ 6 OH/nm^2 by TGA) is considerably larger than the H* adsorption site densities (< 0.3 sites/nm^2) required to describe the surface entropy (**Figure 6**). Given the importance of proton stabilization, a subset of the surface TiOH groups are good candidates for the H* adsorption sites. Titania surfaces are amphiprotic, containing weak acid ($_a$TiOH) and weak base ($_b$TiOH) sites. Proton transfer between these sites yields surface zwitterions, which are likely to have relatively low surface concentrations. Additionally, surface zwitterion generation is a dynamic equilibrium processes and therefore subject to potentially large temperature effects. These are the two key criteria for H* adsorption sites.

Surface zwitterion generation is conceptually equivalent to the well-known temperature effects on water autodissociation (K_w). At 85 °C, $K_w = 6\times10^{-13}$, yielding a neutral pH of 6.1. Thus, the H_3O^+ and OH^- concentrations in water at 85 °C are nearly an order of magnitude higher than at 25 °C. Comparable chemistry between surface TiOH groups should increase surface zwitterion concentration with temperature, providing a plausible mechanism for increasing the H* site density.

We tested this hypothesis using aqueous acid-base titrations of P25 titania suspensions, determining the isoelectric point (IEP) and Brønsted acid-base parameters.[46] From 5-65 °C, the TiO_2 IEP shifts nearly a full pH unit (**Figure 8a**). Measured $_{a}$TiOH and TiOH site densities, are relatively constant (**Figure 8b**); the small changes are attributable to the temperature dependence of water density and dielectric constant.[47] Note the $_{a}$TiOH and $_{b}$TiOH site densities are measured with aqueous titrations, and are therefore subject to surface charging and counterion limitations. Thus the number of proton exchange sites on highly hydroxylated surfaces is generally smaller than the total number of surface hydroxyls measured with TGA.[46]

Measured K_a and K_b values, on the other hand, increase by more than an order of magnitude from 5-65 °C (**Figure 8c**). While solvation energies complicate direct comparisons between aqueous and dry systems, Selloni's work with thin layers of water on anatase [48] suggests trends in surface proton transfer chemistry are similar. In this context, H_2 adsorption can be described as a combination of three reactions: autoionization to form surface zwitterions, adsorption, and spillover:

$$\text{autoionization} \qquad {}_{a}\text{TiOH} + {}_{b}\text{TiOH} \rightleftharpoons {}_{a}\text{TiO}^{-} + {}_{b}\text{TiOH}_2^{+} \tag{3}$$

$$\text{adsorption} \qquad \tfrac{1}{2}\,\text{H}_2 + \text{MSI-OH} \rightleftharpoons \text{H}_{\text{MSI}} \tag{4}$$

$$\text{spillover} \qquad \underline{\text{H}_{\text{MSI}} + {}_{a}\text{TiO}^{-} \rightleftharpoons {}_{a}\text{TiO}^{-}\text{H}^{*} + \text{MSI-OH}} \tag{5}$$

$$\text{net reaction} \qquad \tfrac{1}{2}\,\text{H}_2 + 2\ \text{TiOH} \rightleftharpoons {}_{a}\text{TiO}^{-}\text{H}^{*} + {}_{b}\text{TiOH}_2^{+} \tag{6}$$

There is considerable debate regarding the nature of adsorbed water on TiO_2, particularly if it is dissociated, forming $_{a}$TiOH and $_{b}$TiOH hydroxyls, or remains as intact (strongly bound to Ti sites). We treat the surface as generic TiOH (dissociated water) for simplicity and clarity; however, an autoionization reaction can be applied to either case. Further, the final state of the system (reaction D) is exactly the same regardless of which way the surface and reaction are conceptualized. The key concept is the role of proton transfer in increasing surface zwitterion concentration or stabilizing added protons from H*.

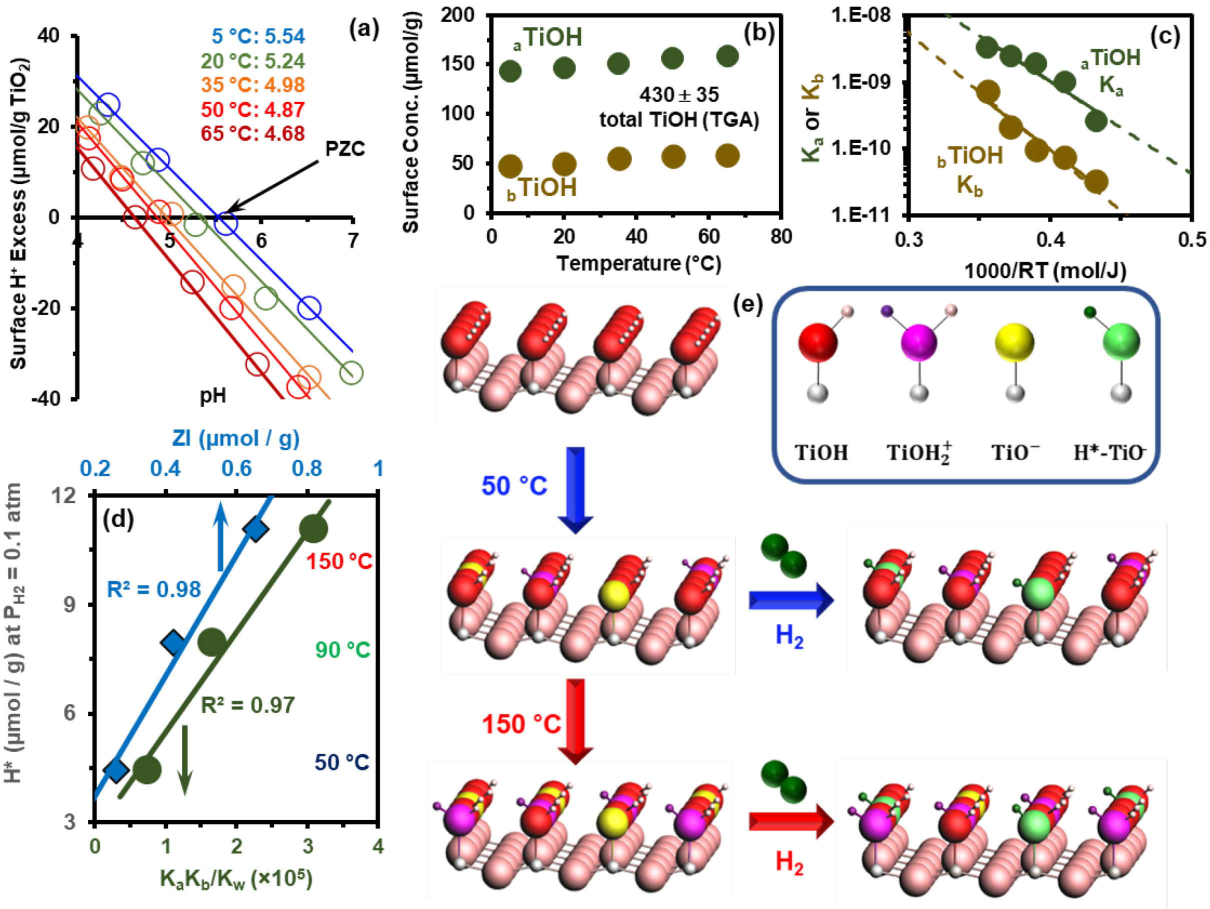

Figure 8. Temperature dependence of TiO$_2$ surface hydroxyl chemistry. (a) IEP measurements from 5-65 °C. **(b)** Surface proton donor ($_a$TiOH) and acceptor ($_b$TiOH) site densities determined from aqueous acid-base titrations. Error bars show the average standard deviation for all measurements in that series. (**c**) K_a and K_b values for $_a$TiOH and $_b$TiOH sites in water, respectively. (**d**) Plot of H* vs. two parameters that scale with the surface zwitterion concentration. (**e**) Schematic representation of temperature induced changes in proton distribution across surface hydroxyls and impact on the number of accessible H* sites.

Combined with the surface entropy discussion, this relatively simple model, shown schematically in **Figure 8e**), accounts for all our observations. The individual isotherm experiments shown in **Figures 1, 3 and 4** probe reactions 4 & 5 only. In these experiments, the adsorption capacity at any given temperature is related to the total number of surface zwitterions present at that temperature. The van't Hoff analysis (**Figure 4f**) quantifies the temperature effects on H* adsorption (reaction 6) and therefore includes increases in the surface zwitterion concentration with increasing temperature. The aqueous titration data can be used to estimate the surface zwitterion concentration (see **Supplementary Discussion**); **Figure 8d** shows H* adsorption is highly correlated to this value. While the absolute value of the surface zwitterion concentration likely changes from aqueous to dry environments, the trends in surface proton transfer chemistry appear to be very similar and explain the increases in H* sites with temperature.[48]

Van Bokhoven's experiments showed reduction of FeO$_x$ via spillover hydrogen is orders of magnitude faster on TiO$_2$ relative to Al$_2$O$_3$.[1] However, spillover on alumina, which has a band gap of ~7 eV, was still observed. Our model also provides a framework for understanding reports of spillover on non-reducible oxides, such as in Van Bokhoven's work. The H* translational entropy, which is the primary thermodynamic driving force for spillover, depends only on the H* surface concentration and is therefore independent of the metal oxide identity. This entropic driving force is balanced against enthalpic energies associated with stabilizing the proton and electron. While H* adsorption on TiO_2 is essentially thermoneutral, adsorption enthalpies are expected to vary significantly with the support identity and must to be tested to better evaluate the generality of the model. However, **Figure 6** shows the translational entropy approaches infinity as the H* coverage approaches zero; consequently, large enthalpic barriers to H* adsorption may be overcome at exceedingly low coverages. Thus, this model provides a clear lens through which future results can be viewed.

Spillover also occurs at higher temperatures on surfaces where few hydroxyl groups are available.[49] While the involvement of surface zwitterions requires the presence of surface hydroxyls, the broader entropic models should apply equally well to dehydroxylated surfaces at higher temperatures. The only real requirement for spillover in our model is the surface must be able to accommodate both protons and electrons; so long as both of these species are stabilized, the basic conclusions regarding entropy should apply to most surfaces. We are now beginning to test to test this hypothesis.

This provides similar insight into the high H_2 evolution activity of Au/TiO_2, despite it being a generally poor hydrogenation catalyst. Zaera's experiments suggested H_2 evolution proceeds through reduction of surface protons at metal or MSI sites on Au/TiO_2 and other doped titanias.[4] Similarly, Selloni showed surface protonation is required for hole transfer to the surface in photocatalytic methanol oxidation.[50] Building on their work, our model and DFT calculations show surface hydroxyls help localize electrons near the support surface, likely slowing electron-hole recombination. Surface proton and electron mobility similarly provide clear transport pathways to rapidly move both to catalytic sites at the MSI.

Conclusions

In summary, our experiments and models show entropy can drive adsorption processes when surface concentrations are low. This provides a robust description of both the nature of and driving force for hydrogen spillover on TiO_2, which is fundamentally driven by large translational entropy at low H* coverage. These thermodynamics are general drivers for spillover and therefore inform other systems, including single atom alloys,[9-11] high entropy alloys, [12] metal-organic frameworks,[13] and metal-semiconductor photoelectrodes.[14] In the specific case of metal oxide supports, where spillover is most prominent on reducible semiconductors, the ability to stabilize added electrons appears to be necessary, but not sufficient. Surface hydroxyls (and/or oxo-groups) play a critical role in stabilizing spillover protons at surface zwitterion sites, while electrons are broadly delocalized. Thus, spillover is an entropy-driven adsorption phenomenon that is intimately tied to the support's ability to stabilize ***both*** surface protons and sub-surface electrons.

Methods

Chemicals

Gases (H_2, N_2) were 5.0 grade supplied by Praxair. Water was purified to a resistivity of 20 MΩ with a Elga Purelab Ultra (Evoqua) system; no additional purification methods were employed. $HAuCl_4\bullet3H_2O$ (99.7%) was purchased from Sigma-Aldrich. NH_4OH (29.3 w/w%) was purchased from Fisher Scientific. Urea (99.5%) was purchased from Acros Organics. Evonik P-25 TiO_2 was generously supplied by Evonik Industries.

Catalyst preparation

Au/TiO_2 catalysts were synthesized in a foil-wrapped flask via urea deposition-precipitation.[35] The desired amount of $HAuCl_4•3H_2O$ and urea (2.52 g, 0.42 M) were added to 250 mL H_2O with stirring. This yellow/orange solution was heated with stirring until the temperature was stable at 80 °C. TiO_2 powder (6 g) was then added and the slurry was stirred at 80 °C for 4 h. After 4 h, the stirring was stopped and the solution was allowed to cool to room temperature, resulting in a yellow paste and clear solution. The solid was isolated via vacuum filtration and washed thoroughly with ~100 mL H_2O followed by ~100 mL 0.1 M NH_4OH, and then H_2O until the filtrate was pH 7; the absence of Au and Cl^- were confirmed with $NaBH_4$ and $AgNO_3$ tests, respectively. The washed solid was dried at room temperature under vacuum for 16 h and stored at 4 °C under air.

The Au/TiO_2 catalysts were prepared by heating the supported precursors in flowing 50% v/v H_2 and N_2. The material was loaded into a tube furnace, heated at 5 °C/min to desired temperature (see **Supplementary Table 1**) and held at the reduction temperature for 1 h, cooled to room temperature and stored at 4 °C under air.

Volumetric H_2 adsorption

All volumetric adsorption experiments were performed on a Micromeritics ASAP 2020. Previously pretreated catalysts (i.e., previously reduced supported Au precursor) were used for H_2 adsorption studies. The sample (200-300 mg) was loaded into a U-tube, evacuated at 150 °C for 1 h and then reduced in flowing H_2 at 150 °C for 1 h to remove any adsorbed oxygen. Following the pretreatment, the sample was evacuated, purged with helium for 30 min, and cooled to the analysis temperature under an active vacuum. A series of two isotherm H_2 adsorption experiments were performed at 60, 90, and 120 °C; the sample was evacuated to at least 10 µm Hg for 1 h at the adsorption temperature between isotherms.

We note any adsorbed oxygen in the system must be removed before reversible H_2 adsorption can be observed either via volumetric adsorption or with FTIR spectroscopy. Once care is taken to remove adsorbed oxygen, the first and the second isotherms are essentially indistinguishable. Therefore, for all further volumetric adsorption measurements described hereafter, reported hydrogen uptakes were determined by averaging the first and second isotherms at each pressure point.

FTIR Spectroscopy

Infrared spectra were collected on a Thermo Nicolet Nexus 470 FTIR spectrometer in a home-built heated (20-300 °C) transmission flow cell. Gas flow rates were controlled using rotameters calibrated with a bubble flowmeter. Water in the feed gases was minimized by passing the reactive gas through a dry ice-isopropanol moisture trap immediately prior to entering the IR cell. For H_2 adsorption experiments, ~40-50 mg of catalyst sample was pressed (3 tons of pressure for 10 s) into a 13 mm circular pellet, which was mounted in the flow cell. The sample pellet was pretreated under 25 sccm of N_2 at 300 °C for 1 h to eliminate surface carbonates, and then cooled to 50 °C. The vapor pressure of water at -78 °C is 0.5 mTorr (660 ppb). Even with the dry ice-isopropanol bath, sub-ppm levels of residual water from the gas stream adsorb on the surface at lower temperatures. We allowed the surface water coverage to equilibrate until the water bending band at 1620 cm^{-1} was stable before conducting further experiments. Based on our previous work and the absorbance of the δ_{HOH} bending vibration, we estimate the surface water coverage to be around 2-3 H_2O molecules / nm^2. [21]

After stabilization of the water bending mode, a mixture of 20 sccm H_2 and 25 sccm N_2 was flowed over the catalyst at 50 °C for one hour to ensure no weakly adsorbed O_2 remained on the pellet. Catalysts were kept under N_2 flow to ensure the weakly adsorbed H_2 is removed. H_2 adsorption experiments were then performed at desired temperatures by flowing the desired ratio of H_2 and N_2 over the catalyst.

Transmission Electron Microscopy

Gold particle sizes were determined with transmission electron microscopy. Catalysts were imaged with scanning/transmission electron microscopy (STEM) using an FEI Talos F200X microscope at an accelerating voltage of 200 kV. A small quantity of each sample was crushed in an agate mortar and dispersed in ethanol with sonication. A few drops of this suspension were placed on a Cu TEM grid (Ted Pella, Inc.) and allowed to dry before inserting into the microscope for analysis. The number-averaged diameter for Au nanoparticles was determined with ImageJ from the measurement of >200 particles (**Supplementary Figure 1**). **Supplementary Table 1** compiles TEM, and BET characterization data for the catalysts studied in this work. Error bars associated with the diameter represent the standard deviation of the distribution.

Data Availability

Raw data is available through ScholarSphere, Penn State's open access repository at https://scholarsphere.psu.edu/.

Acknowledgements

The authors gratefully acknowledge the Department of Energy Basic Energy Sciences Program (DE-SC0022053 and DE-SC0016192) for primary support of this work. Preliminary experiments were supported by the National Science Foundation (CBET-1803769, 1803808, and 2102430) and the Research Corporation for Science Advancement. The computational work was completed with resources provided by the Research Computing Data Core at the University of Houston. We thank Prof. Mike Janik at Penn State for invaluable discussions and Dr. Tianze Xie for his assistance in collecting TEM data.

Author Contributions

Conceptualization: BDC, TNW, AMS
Formal Analysis: AMS, TNW, TYY, SW, KBSK, LCR,
Funding Acquisition: BDC, LCG, RMR
Investigation: AMS, TNW, TYY, LCR, SW, KBSK
Methodology: AMS, TNW, TYY, SG
Project Administration: BDC
Supervision: BDC, AMS, LCG
Visualization: AMS, TNW, TYY, SW
Writing – original draft: BDC & AMS
Writing – review & editing: TNW, RMR, LCG, SW, KBSK

Competing Interests

The authors declare no competing interests.

Figure Captions

Figure 1. Temperature and particle size effects on H_2 adsorption. (a) H_2 equilibrium adsorption isotherms on Au/TiO_2 as a function of temperature and P_{H2}. Error bars show a 15% relative standard deviation, which is the determined uncertainty for six isotherm measurements at each temperature. **(b)** Total H_2 adsorption normalized to the number of MSI sites as a function of Au particle size. At a constant Au wt. %, H_2 adsorption per adsorption site increases with Au particle size. Error bars show standard deviations from TEM data (x-axis) and adsorption isotherm data (y-axis). Particle size calculations are detailed in the **Supplementary Methods**.

Figure 2. Au loading effects on H_2 adsorption and spillover. (a) H_2 adsorption isotherms (90 °C) on catalysts with comparable Au particle size (~3 nm), but variable Au loading. Total H_{ads} is normalized to the number of surface Au atoms; the ratio of H_{ads}:Au_{surf} changes with Au loading indicating H is not transferred to Au. Error bars show the standard deviation based on at least four isotherm measurements. **(b)** H* adsorption isotherms; data from 2A with adsorption attributable to the MSI sites subtracted. **(c & d)** Temperature effects on H* adsorption; data from 1A with adsorption attributable to the MSI sites subtracted plotted on linear (c and logarithmic (d axes. Lines are fits to two-site Langmuir models.

Figure 3. Schematic showing H_2 adsorption at the MSI. Beginning from the left of the figure, H_2 adsorbs at the Au/TiO_2 metal-support interface (MSI). The species adsorbed at the interface (H_{MSI}), is described as a proton interacting with a basic MSI hydroxyl group and an electron delocalized across the associated Ti-O antibonding orbital, nearby support atoms, and the Au. Once the MSI hydroxyls are saturated with HMSI, H-atom equivalents (H*) are transferred to the support. The highly mobile H* species are similar to HMSI, consisting of a proton interacting with a surface TiOH and an electron in surface conduction band states delocalized across the TiOH and neighboring support atoms.

Figure 4. H* Adsorption Thermodynamics. (**a**) Linearized Langmuir plot for H* on 2.8 nm-1% Au/TiO_2 at 90 °C. Langmuir parameters were extracted from sliding linear fits as shown. (**b**) Extracted Langmuir parameters from (A) plotted as a function of P_{H2}. Data show the adsorption equilibrium has a strong surface concentration dependence. (**c**) ΔG_{H*} values at 90 °C for three catalysts as a function of surface concentration. (**d**) ΔG_{H*} values for 2.8 nm-1% Au/TiO_2 at three temperatures. (**e**) Data from panels (C) and (D) plotted versus P_{H2}. **(f)** Langmuir parameter temperature dependence. Parameters extracted at ~25 Torr H_2; symbols average 5 data points measured over 5 different catalysts having different Au loadings and average particle sizes between 2.5 and 4 nm. Error bars show standard deviations for at least 5 determinations over 5 different catalysts with varying Au loading and particle size (minimum 15 measurements); error bars for K^*_{25} values are smaller than the symbols (RSD: 12%).

Figure 5. Entropy diagram for H* adsorption at 25 °C. Energy diagram showing changes in standard entropy for H_2 dissociation and adsorption on a solid. The entropy loss due to H atom immobilization on the surface is balanced offset by the entropy gains due to H-H bond dissociation and H surface entropy (translational, configurational, and vibrational entropy). When the standard surface entropy of the adsorbed H atoms exceeds 64 J/molK,H adsorption is entropically favorable.

Figure 6. Entropic contributions to hydrogen spillover energetics. **(a)** Experimentally determined (symbols) and calculated (lines) S_{H*} values based only on translational entropy contributions ($_{tr}S_{H*}$). The horizontal line approximates the minimum S_{H*} required for a net

favorable adsorption entropy ($\Delta S_{H^*} = 0$) at 25 °C. The inset shows the same plot at experimentally relevant H* surface densities. **(b)** Experimentally determined (symbols) and calculated (lines) S_{H^*} values including translational and configurational entropy contributions ($_{(tr+config)}S_{H^*}$), see the **Supplementary Discussion** for details. The lines show the calculated S_{H^*} values at a specific temperature using a fitted number of adsorption sites (n_s), which is required to determine the fractional coverage see equation (2).

Figure 7. DFT model for H* adsorbed on rutile (110) and anatase (001). DFT calculations for H* adsorbed on fully hydroxylated rutile (110) at 0.1 H*/nm^2 (a & b), 2.5 H*/nm^2 (c & d), and anatase at 1.7 H*/nm^2 (e & f). Panels a, c, and e show changes in electron density; panels b, d, and f show changes in electron spin density.

Figure 8. Temperature dependence of TiO_2 surface hydroxyl chemistry. (a) IEP measurements from 5-65 °C. Error bars show the average standard deviation for all measurements in that series ((**b**) determined surface proton donor ($_a$TiOH) and acceptor ($_b$TiOH) site densities in water (error bars show standard deviations for a minimum of three experiments); (**c**) K_a and K_b values for $_a$TiOH and $_b$TiOH sites in water, respectively. (**d**) Schematic representation of temperature induced changes in proton distribution across surface hydroxyls and impact on the number of accessible H* sites.

References

1 Karim, W. *et al.* Catalyst support effects on hydrogen spillover. *Nature* **541**, 68-71 (2017). https://doi.org:10.1038/nature20782

2 Hülsey, M. J., Fung, V., Hou, X., Wu, J. & Yan, N. Hydrogen Spillover and Its Relation to Hydrogenation: Observations on Structurally Defined Single-Atom Sites**. *Angewandte Chemie International Edition* **61**, e202208237 (2022). https://doi.org:https://doi.org/10.1002/anie.202208237

3 Prins, R. Hydrogen Spillover. Facts and Fiction. *Chemical Reviews* **112**, 2714-2738 (2012). https://doi.org:10.1021/cr200346z

4 Joo, J. B. *et al.* Promotion of atomic hydrogen recombination as an alternative to electron trapping for the role of metals in the photocatalytic production of H₂. *Proceedings of the National Academy of Sciences* **111**, 7942-7947 (2014). https://doi.org:doi:10.1073/pnas.1405365111

5 Primo, A., Corma, A. & García, H. Titania supported gold nanoparticles as photocatalyst. *Physical Chemistry Chemical Physics* **13**, 886-910 (2011). https://doi.org:10.1039/C0CP00917B

6 Panayotov, D. A. & Morris, J. R. Surface chemistry of Au/TiO2: Thermally and photolytically activated reactions. *Surface Science Reports* **71**, 77-271 (2016). https://doi.org:https://doi.org/10.1016/j.surfrep.2016.01.002

7 Chen, X., Liu, L., Yu, P. Y. & Mao, S. S. Increasing Solar Absorption for Photocatalysis with Black Hydrogenated Titanium Dioxide Nanocrystals. *Science* **331**, 746-750 (2011). https://doi.org:doi:10.1126/science.1200448

8 Lu, Y. *et al.* Self-hydrogenated shell promoting photocatalytic H2 evolution on anatase TiO2. *Nature Communications* **9**, 2752 (2018). https://doi.org:10.1038/s41467-018-05144-1

9 Lucci, F. R. *et al.* Selective hydrogenation of 1,3-butadiene on platinum-copper alloys at the single-atom limit. *Nat. Commun.* **6** (2015). https://doi.org:10.1038/ncomms9550

10 Darby, M. T., Stamatakis, M., Michaelides, A. & Sykes, E. C. H. Lonely Atoms with Special Gifts: Breaking Linear Scaling Relationships in Heterogeneous Catalysis with Single-Atom Alloys. *The Journal of Physical Chemistry Letters* **9**, 5636-5646 (2018). https://doi.org:10.1021/acs.jpclett.8b01888

11 O'Connor, C. R. *et al.* Facilitating hydrogen atom migration via a dense phase on palladium islands to a surrounding silver surface. *Proceedings of the National Academy of Sciences* **117**, 22657-22664 (2020). https://doi.org:10.1073/pnas.2010413117

12 Mori, K. *et al.* Hydrogen spillover-driven synthesis of high-entropy alloy nanoparticles as a robust catalyst for CO2 hydrogenation. *Nature Communications* **12**, 3884 (2021). https://doi.org:10.1038/s41467-021-24228-z

13 Li, Y. & Yang, R. T. Significantly Enhanced Hydrogen Storage in Metal-Organic Frameworks via Spillover. *J. Am. Chem. Soc.* **128**, 726-727 (2006). https://doi.org:10.1021/ja056831s

14 Esposito, D. V., Levin, I., Moffat, T. P. & Talin, A. A. H2 evolution at Si-based metal-insulator-semiconductor photoelectrodes enhanced by inversion channel charge collection and H spillover. *Nat. Mater.* **12**, 562-568 (2013). https://doi.org:10.1038/nmat3626

15 Kumaravel, V., Mathew, S., Bartlett, J. & Pillai, S. C. Photocatalytic hydrogen production using metal doped TiO2: A review of recent advances. *Applied Catalysis B: Environmental* **244**, 1021-1064 (2019). https://doi.org:https://doi.org/10.1016/j.apcatb.2018.11.080

16 Sampath, A. *et al.* Spectroscopic Evidence for the Involvement of Interfacial Sites in O–O Bond Activation over Gold Catalysts. *ACS Catalysis* **12**, 9549-9558 (2022). https://doi.org:10.1021/acscatal.2c02076

17 Cargnello, M. *et al.* Control of Metal Nanocrystal Size Reveals Metal-Support Interface Role for Ceria Catalysts. *Science* **341**, 771-773 (2013). https://doi.org:10.1126/science.1240148

18 Frey, H., Beck, A., Huang, X., Bokhoven, J. A. v. & Willinger, M. G. Dynamic interplay between metal nanoparticles and oxide support under redox conditions. *Science* **376**, 982-987 (2022). https://doi.org:doi:10.1126/science.abm3371

19 Rolison, D. R. *et al.* Power of Aerogel Platforms to Explore Mesoscale Transport in Catalysis. *ACS Appl. Mater. Interfaces* **12**, 41277-41287 (2020). https://doi.org:10.1021/acsami.0c10004

20 Sankar, M. *et al.* Role of the Support in Gold-Containing Nanoparticles as Heterogeneous Catalysts. *Chemical Reviews* **120**, 3890-3938 (2020). https://doi.org:10.1021/acs.chemrev.9b00662

21 Saavedra, J., Doan, H. A., Pursell, C. J., Grabow, L. C. & Chandler, B. D. The critical role of water at the gold-titania interface in catalytic CO oxidation. *Science* **345**, 1599-1602 (2014). https://doi.org:10.1126/science.1256018

22 Yuan, W. *et al.* In situ manipulation of the active Au-TiO₂ interface with atomic precision during CO oxidation. *Science* **371**, 517-521 (2021). https://doi.org:doi:10.1126/science.abe3558

23 Green, I. X., Tang, W., Neurock, M. & Yates, J. T., Jr. Spectroscopic Observation of Dual Catalytic Sites During Oxidation of CO on a Au/TiO2 Catalyst. *Science* **333**, 736-739 (2011). https://doi.org:10.1126/science.1207272

24 Corma, A. & Garcia, H. Supported gold nanoparticles as catalysts for organic reactions. *Chemical Society Reviews* **37**, 2096-2126 (2008).

25 Hashmi, S. K. & Hutchings Graham, J. Gold catalysis. *Angewandte Chemie (International ed. in English)* **45**, 7896-7936 (2006).

26 Zhang, Y., Cui, X., Shi, F. & Deng, Y. Nano-Gold Catalysis in Fine Chemical Synthesis. *Chemical Reviews* **112**, 2467-2505 (2012). https://doi.org:10.1021/cr200260m

27 Ojeda, M. & Iglesia, E. Formic Acid Dehydrogenation on Au-Based Catalysts at Near-Ambient Temperatures. *Angewandte Chemie International Edition* **48**, 4800-4803 (2009). https://doi.org:https://doi.org/10.1002/anie.200805723

28 Rodriguez, J. A. *et al.* Activity of CeO_{<i>x</i>} and TiO_{<i>x</i>} Nanoparticles Grown on Au(111) in the Water-Gas Shift Reaction. *Science* **318**, 1757-1760 (2007). https://doi.org:doi:10.1126/science.1150038

29 Shekhar, M. *et al.* Size and Support Effects for the Water–Gas Shift Catalysis over Gold Nanoparticles Supported on Model Al2O3 and TiO2. *Journal of the American Chemical Society* **134**, 4700-4708 (2012). https://doi.org:10.1021/ja210083d

30 Mitsudome, T. & Kaneda, K. Gold nanoparticle catalysts for selective hydrogenations. *Green Chemistry* **15**, 2636-2654 (2013). https://doi.org:10.1039/C3GC41360H

31 Sault, A. G., Madix, R. J. & Campbell, C. T. Adsorption of oxygen and hydrogen on gold(110)-(1 × 2). *Surf. Sci.* **169**, 347 (1986). https://doi.org:10.1016/0039-6028(86)90616-3

32 Whittaker, T. *et al.* H2 Oxidation over Supported Au Nanoparticle Catalysts: Evidence for Heterolytic H2 Activation at the Metal–Support Interface. *Journal of the American Chemical Society* **140**, 16469-16487 (2018). https://doi.org:10.1021/jacs.8b04991

33 Sravan Kumar, K. B., Whittaker, T. N., Peterson, C., Grabow, L. C. & Chandler, B. D. Water Poisons H2 Activation at the Au–TiO2 Interface by Slowing Proton and Electron Transfer between Au and Titania. *Journal of the American Chemical Society* **142**, 5760-5772 (2020). https://doi.org:10.1021/jacs.9b13729

34 Mahdavi-Shakib, A., Rich, L. C., Whittaker, T. N. & Chandler, B. D. Hydrogen Adsorption at the Au/TiO2 Interface: Quantitative Determination and Spectroscopic Signature of the Reactive Interface Hydroxyl Groups at the Active Site. *ACS Catalysis* **11**, 15194-15202 (2021). https://doi.org:10.1021/acscatal.1c04419

35 Mahdavi-Shakib, A. *et al.* Kinetics of H2 Adsorption at the Metal–Support Interface of Au/TiO2 Catalysts Probed by Broad Background IR Absorbance. *Angewandte Chemie International Edition* **60**, 7735-7743 (2021). https://doi.org:https://doi.org/10.1002/anie.202013359

36 Honkala, K. *et al.* Ammonia Synthesis from First-Principles Calculations. *Science (Washington, DC, U. S.)* **307**, 555-558 (2005). https://doi.org:10.1126/science.1106435

37 Rekharsky, M., Inoue, Y., Tobey, S., Metzger, A. & Anslyn, E. Ion-Pairing Molecular Recognition in Water: Aggregation at Low Concentrations That Is Entropy-Driven. *Journal of the American Chemical Society* **124**, 14959-14967 (2002). https://doi.org:10.1021/ja020612e

38 Hartshorn, H., Pursell, C. J. & Chandler, B. D. Adsorption of CO on Supported Gold Nanoparticle Catalysts: A Comparative Study. *J. Phys. Chem. C* **113**, 10718-10725 (2009). https://doi.org:https://doi.org/10.1021/jp902553n

39 Campbell, C. T., Sprowl, L. H. & Árnadóttir, L. Equilibrium Constants and Rate Constants for Adsorbates: Two-Dimensional (2D) Ideal Gas, 2D Ideal Lattice Gas, and Ideal Hindered Translator Models. *The Journal of Physical Chemistry C* **120**, 10283-10297 (2016). https://doi.org:10.1021/acs.jpcc.6b00975

40 Campbell, C. T. & Sellers, J. R. V. The Entropies of Adsorbed Molecules. *Journal of the American Chemical Society* **134**, 18109-18115 (2012). https://doi.org:10.1021/ja3080117

41 Campbell, C. T. & Sellers, J. R. V. Enthalpies and entropies of adsorption on well-defined oxide surfaces: Experimental measurements. *Chem. Rev. (Washington, DC, U. S.)* **113**, 4106-4135 (2013). https://doi.org:10.1021/cr300329s

42 Savara, A., Schmidt, C. M., Geiger, F. M. & Weitz, E. Adsorption Entropies and Enthalpies and Their Implications for Adsorbate Dynamics. *J. Phys. Chem. C* **113**, 2806-2815 (2009). https://doi.org:10.1021/jp806221j

43 Collinge, G. *et al.* Effect of Collective Dynamics and Anharmonicity on Entropy in Heterogeneous Catalysis: Building the Case for Advanced Molecular Simulations. *ACS Catal.* **10**, 9236-9260 (2020). https://doi.org:10.1021/acscatal.0c01501

44 Vannice, M. A., Hyun, S. H., Kalpakci, B. & Liauh, W. C. Entropies of adsorption in heterogeneous catalytic reactions. *Journal of Catalysis* **56**, 358-362 (1979). https://doi.org:https://doi.org/10.1016/0021-9517(79)90128-3

45 Spreafico, C., Karim, W., Ekinci, Y., van Bokhoven, J. A. & VandeVondele, J. Hydrogen Adsorption on Nanosized Platinum and Dynamics of Spillover onto Alumina and Titania. *The Journal of Physical Chemistry C* **121**, 17862-17872 (2017). https://doi.org:10.1021/acs.jpcc.7b03733

46 Yun, T. Y. & Chandler, B. D. Surface Hydroxyl Chemistry of Titania- and Alumina-Based Supports: Quantitative Titration and Temperature Dependence of Surface Brønsted Acid–Base Parameters. *ACS Applied Materials & Interfaces* **15**, 6868-6876 (2023). https://doi.org:10.1021/acsami.2c20370

47 Luetzenkirchen, J. & Finck, N. Treatment of temperature dependence of interfacial speciation by speciation codes and temperature congruence of oxide surface charge. *Appl. Geochem.* **102**, 26-33 (2019). https://doi.org:10.1016/j.apgeochem.2018.12.023

48 Lu, Y. *et al.* Self-hydrogenated shell promoting photocatalytic H2 evolution on anatase TiO2. *Nat. Commun.* **9**, 1-9 (2018). https://doi.org:10.1038/s41467-018-05144-1

49 Beaumont, S. K., Alayoglu, S., Specht, C., Kruse, N. & Somorjai, G. A. A Nanoscale Demonstration of Hydrogen Atom Spillover and Surface Diffusion Across Silica Using the Kinetics of CO2 Methanation Catalyzed on Spatially Separate Pt and Co Nanoparticles. *Nano Letters* **14**, 4792-4796 (2014). https://doi.org:10.1021/nl501969k

50 Setvin, M. *et al.* Methanol on Anatase TiO2 (101): Mechanistic Insights into Photocatalysis. *ACS Catal.* **7**, 7081-7091 (2017). https://doi.org:10.1021/acscatal.7b02003